

RESEARCH ARTICLE

# A generalized framework for reduced-order modeling of a wind turbine wake

Nicholas Hamilton<sup>1,2</sup>  | Bianca Viggiano<sup>1</sup> | Marc Calaf<sup>3</sup> | Murat Tutkun<sup>4,5</sup> | Raúl Bayoán Cal<sup>1</sup>

<sup>1</sup>Mechanical and Materials Engineering, Portland State University, Oregon, USA

<sup>2</sup>National Renewable Energy Laboratory, Colorado, USA

<sup>3</sup>Mechanical Engineering, University of Utah, Utah, USA

<sup>4</sup>Department of Wind Technology, IFE, Kjeller, Norway

<sup>5</sup>Department of Mathematics, University of Oslo, Oslo, Norway

## Correspondence

Nicholas Hamilton, National Renewable Energy Laboratory, Colorado, USA.  
Email: nicholas.hamilton@nrel.gov

## Funding information

National Science Foundation, Grant/Award Number: NSF-ECCS-1032647 and NSF-CBET-1034581; National Science Foundation IGERT, Grant/Award Number: 0966376; Research Council of Norway, Grant/Award Number: 231491

## Abstract

A reduced-order model for a wind turbine wake is sought from large eddy simulation data. Fluctuating velocity fields are combined in the correlation tensor to form the kernel of the proper orthogonal decomposition (POD). Proper orthogonal decomposition modes resulting from the decomposition represent the spatially coherent turbulence structures in the wind turbine wake; eigenvalues delineate the relative amount of turbulent kinetic energy associated with each mode. Back-projecting the POD modes onto the velocity snapshots produces dynamic coefficients that express the amplitude of each mode in time. A reduced-order model of the wind turbine wake (wakeROM) is defined through a series of polynomial parameters that quantify mode interaction and the evolution of each POD mode coefficients. The resulting system of ordinary differential equations models the wind turbine wake composed only of the large-scale turbulent dynamics identified by the POD. Tikhonov regularization is used to recalibrate the dynamical system by adding additional constraints to the minimization seeking polynomial parameters, reducing error in the modeled mode coefficients. The wakeROM is periodically reinitialized with new initial conditions found by relating the incoming turbulent velocity to the POD mode coefficients through a series of open-loop transfer functions. The wakeROM reproduces mode coefficients to within 25.2%, quantified through the normalized root-mean-square error. A high-level view of the modeling approach is provided as a platform to discuss promising research directions, alternate processes that could benefit stability and efficiency, and desired extensions of the wakeROM.

## KEYWORDS

dynamical system, proper orthogonal decomposition, reduced-order model, wind turbine wake

## 1 | INTRODUCTION

Performance of wind farms is highly correlated with the wake following a given wind turbine.<sup>1,2</sup> However, for the sake of design efficiency, wakes and wind plants are typically modeled with simplified engineering or empirical relationships. Wind turbine wakes are highly variable, combining effects from the atmospheric boundary layer, interacting with large rotating structures, and often subject to wake-to-wake interaction within a wind plant.<sup>3</sup> Further, wakes evolving from individual turbines are asymmetrical due to the inherent shear in the atmospheric boundary layer and reflect the specific nature of incoming inflow events that vary significantly with diurnal and seasonal cycles and affect the performance of other turbines in a wind plant.<sup>4</sup> Given the complexity of the wind turbine wake, a computationally efficient means of correctly modeling wake dynamics and interaction is crucial to meet the rapid pace at which wind energy is being adopted globally and to address persistent wind plant underperformance.

Reduced-order modeling describes a wide range of approaches that approximate complex system dynamics of large or infinite degrees of freedom with a limited, and more manageable, number of degrees of freedom. For applications in turbulence, the goal is typically to simplify the Navier-Stokes equations, by isolating the important dynamics for a given flow with an effective use of computational resources. Of these approaches, modal decomposition methods are frequently selected as they add definition and organization to the vector space of the input information and offer intuitive means of filtering or truncation. The proper orthogonal decomposition (POD) is a widely-used method as it represents the optimal organization of

turbulence structures based on energy.<sup>5</sup> With careful selection of the point of truncation of the mode basis, it is possible to retain the most dominant dynamics in the system with the least number of modes.<sup>6</sup> For turbulent flow data of high spatial resolution, the classical POD presented by Lumley<sup>7</sup> is not as computationally efficient as the method of snapshots by Sirovich.<sup>8</sup> The POD has been used in the analysis of wind energy for field measurements,<sup>9</sup> experiments,<sup>10,11</sup> and simulations.<sup>12–14</sup>

Galerkin projection is widely used to reconcile the modal basis with a governing behavior law, resulting in a minimal set of ordinary differential equations.<sup>15</sup> The Galerkin-POD procedure was first used in turbulent shear flow modeling<sup>16</sup> and has since been extended to many flow scenarios, such as mixing layers and wakes,<sup>17,18</sup> compressible flows,<sup>19</sup> and bluff body wakes and aerodynamics,<sup>20,21</sup> among others. Stability is a common difficulty with reduced-order models (ROMs), typically arising from truncating the dynamics to exclude higher-order, dissipative contributions to the overall flow. Often, additional turbulence terms, such as eddy viscosities, pressure-strain correlations, and diffusion models are introduced to the system to add stability.<sup>20,22,23</sup> Ultimately, stable ROMs require a substantial amount of training data and are often most effectively derived from data intensive numerical simulations. In an experimental framework, strong closure assumptions are often used to account for incomplete or insufficiently resolved process due to lack of required data.<sup>17,24</sup> Brunton and Noack<sup>25</sup> provide a thorough review of closure problems for dynamical system modeling of turbulence and the challenges that remain in deploying prediction and flow control strategies.

An approach to reduced-order modeling was defined in analogy to the Galerkin-POD by Perret et al,<sup>26</sup> wherein the time-dependent mode coefficients are used directly in the formation of the dynamical system. In this approach, simultaneous realizations of the coefficients and their respective time derivatives are required to describe the evolution of the system. Proper orthogonal decomposition coefficients are combined through a least-squares polynomial fit including constant, linear, quadratic, and cubic parameters. Linear and quadratic parameters are analogous to those produced through the Galerkin-POD method accounting for mode interaction associated with the viscous and convective terms of the Navier-Stokes equations. Constant and cubic parameters added to the ROM through the least-squares polynomial fit add stability to the dynamical system,<sup>17</sup> but do not issue from projecting the modal basis onto the Navier-Stokes equations, as is the case with the Galerkin-POD method. The data-driven system was combined with a dynamic reinitialization technique by Hamilton et al<sup>27</sup> for a turbulent channel flow, demonstrating the effectiveness of the technique for making estimates of the turbulence field far beyond the time span of the training data.

Data-driven ROMs are promising for predictive methodologies and flow control applications due to the simplified definition of turbulence dynamics, speed of calculation, and portability to control methods,<sup>28</sup> even without explicit knowledge of the underlying flow physics. Because the computational cost is low for data-driven models, composition with a larger range of degrees of freedom is feasible, enabling one to account for a broader range of system dynamics.<sup>27,29–31</sup> Auxiliary turbulence terms and physical mechanisms sought in numerous Galerkin-POD studies<sup>20,22,23</sup> are taken implicitly from the dynamics of the input data in this application. Data-driven methods that do not require knowledge of the underlying physics are frequently classified as model-free systems.

Numerical solution of ordinary differential equations can lead to the propagation of error that can cause divergence of the system. This is a common issue in POD-based dynamical systems. Often, exclusion of higher-order modes that account for dissipation and diffusion mechanisms changes the energy balance of the system.<sup>32</sup> Other potential pitfalls with POD-based systems come from limited input data, which produce basis modes that are not statistically converged, and sensitivity of the dynamical system to initial conditions,<sup>25</sup> which can lead to skewed descriptions of the flow field. Error propagation in reduced-order models can be mitigated through a number of recalibration techniques and for a wide range of dynamical systems, including model-free and purely empirical models.<sup>22,33–37</sup>

Couplet et al<sup>32</sup> introduced a calibration step to the POD-Galerkin coefficients, seeking to minimize the error observed between the behavior of the input data and that of the dynamical system. Tikhonov regularization was further used to recalibrate the parameters quantifying mode interaction, which adds stability to reduced-order turbulence models,<sup>31</sup> finding that the proposed methods to be applicable to unstable POD-Galerkin systems. The computational cost of construction of the data-driven dynamical systems is generally less than the cost associated with POD-Galerkin calculations for transitional or turbulent flows.<sup>25,31</sup> Cordier et al<sup>35</sup> compared multiple methods of calibration implemented for an improved reduced-order model accuracy. Numerical experiments indicate that, with respect to normalized errors, the Tikhonov regularization outperforms other effective methods, seeking the optimal balance between model stability and variability.<sup>38</sup>

To make best use of wind energy resources, wind farm designers and engineers require sophisticated tools that accurately simulate the complicated interactions of the turbines with the atmospheric boundary layer. Wind turbine wakes play a dual role in wind farms as a source of increased turbulence and fatigue loads on blades and as a mechanism responsible for resupplying the wind plant with high-momentum flow.<sup>2,39</sup> Additionally, turbulent wake interaction in a wind farm increases operation and maintenance costs and decreases the capacity factor of constituent turbines. To optimize the performance of new and existing wind energy resources, a new generation of control and optimization strategies is necessary that accounts for the global aerodynamics of the wind farm system. In this paper, a large eddy simulation (LES) framework is used to describe the turbulent wind turbine wake (Section 3). Dynamics are subsequently isolated with the proper orthogonal decomposition (Section 2.1) and used to formulate a reduced-order model (Section 2.2). The resulting dynamical system is subject to instabilities endogenous to the turbulence and introduced during the numerical solution of the system. However, when recalibrated through Tikhonov regularization, the wakeROM becomes more stable and capable of producing accurate estimates of the wind turbine wake. Incoming flow events are related to the POD mode coefficients through a system of transfer functions and periodically offer new initial conditions to the wakeROM. Providing wind turbine operating conditions as feedback parameters, the data-driven dynamical system here may be concatenated in series, offering a means of control and optimization for global wind farm power

production. Components of the wakeROM workflow that represent paths for future development or additional investigation are discussed in Section 5, and conclusions of the current work are presented in Section 6.

## 2 | THEORY

### 2.1 | Snapshot proper orthogonal decomposition

For data with fine spatial resolution, the method of snapshots<sup>8</sup> provides a computational advantage over the classical POD.<sup>7</sup> The following theoretical development outlines the definition of a basis of modes (or eigenfunctions) ordered by their projection onto the fluctuating velocity correlation tensor. The eigenvalue associated with each mode delineates the energy that a particular structure conveys in the turbulence kinetic energy (TKE) budget of the sampled data. Math symbols in bold represent vectorial quantities, while symbols in plain text are scalars. The flow field is a stochastic function of space and time. Velocity snapshots are denoted as  $\mathbf{u}(\mathbf{x}, t^n)$ , where  $\mathbf{x}$  and  $t^n$  refer to the spatial coordinate and time at sample  $n$ , respectively, over  $N$  total snapshots  $t^0 \leq t^n \leq t^N$ .

Stated simply, the POD seeks a set of modes and coefficients that optimally describes the kernel of the decomposition, in this case, the two-point cross-correlation tensor  $\mathbf{R}$ . All three Cartesian components of the fluctuating velocity field are used to define the correlation tensor as

$$\mathbf{R}(\mathbf{x}, \mathbf{x}') = \frac{1}{N} \sum_{n=1}^N \mathbf{u}(\mathbf{x}, t^n) \mathbf{u}^T(\mathbf{x}', t^n), \quad (1)$$

where  $N$  signifies the number of snapshots and the prime represents the spatial coordinate of another point in the domain. Proper orthogonal decomposition modes take the form  $\Phi = \sum_{n=1}^N \mathcal{A}(t^n) \mathbf{u}(\mathbf{x}, t^n)$ , where  $\Phi$  represent projections onto the stochastic velocity field in a mean square sense and  $\mathcal{A}$  are coefficients quantifying the projection onto each velocity snapshot. The correlation tensor and ansatz of the modes are substituted into a Fredholm integral equation of the second kind,

$$\int_D \mathbf{R}(\mathbf{x}, \mathbf{x}') \Phi(\mathbf{x}') d\mathbf{x}' = \lambda \Phi(\mathbf{x}), \quad (2)$$

where  $D$  is the physical measurement domain and  $\lambda$  are eigenvalues that delineate the corresponding contribution of each mode to the total integrated TKE. Equation 2 is discretized and solved numerically as an eigenvalue problem. Modes are normalized by their respective  $L^2$ -norm by convention,

$$\Phi^{(i)}(\mathbf{x}) = \frac{\sum_{n=1}^N \mathcal{A}^{(i)}(t^n) \mathbf{u}(\mathbf{x}, t^n)}{\left\| \sum_{n=1}^N \mathcal{A}^{(i)}(t^n) \mathbf{u}(\mathbf{x}, t^n) \right\|}, \quad i = 1, \dots, N. \quad (3)$$

Proper orthogonal decomposition mode coefficients  $a_i(t)$  associated with each mode are sought by back-projecting the set of stochastic velocity fields onto the basis of POD modes and integrating over  $D$ ,

$$a_i(t) = \int_D \mathbf{u}(\mathbf{x}, t) \Phi^{(i)}(\mathbf{x}) d\mathbf{x}. \quad (4)$$

With spatially coherent POD modes and the respective time-varying coefficients, the velocity field may be represented through the relationship,

$$\mathbf{u}(\mathbf{x}, t) = \sum_{i=1}^N a_i(t) \Phi^{(i)}(\mathbf{x}). \quad (5)$$

By convention, POD modes themselves carry no units. It is only in combination with their respective coefficients that they represent physical contributions to the velocity field. Truncating the basis of POD modes before reconstructing velocity snapshots as in Equation 5 results in a filtered description of the turbulence. Low-rank modes are taken to be the most energetic and anisotropic structures in the flow field; intermediate and high-rank POD modes account for turbulence kinetic energy that is more homogeneously distributed and more isotropic, detailed in Hamilton et al.<sup>40</sup> The point at which the POD basis is truncated is typically determined by choosing a desired level of the TKE according to the eigenvalues,  $\lambda$ .

A quantitative description of the accuracy of a low-order description of the turbulence field through the POD as by Equation 5 is achieved through the normalized root-mean-square error (NRMSE), calculated as,

$$\text{NRMSE}(\hat{g}) = 100 \times \frac{\sqrt{(g - \hat{g})^2}}{\max(g) - \min(g)}, \quad (6)$$

where  $g$  is a reference signal and  $\hat{g}$  is the test signal. This method is used for error quantification throughout the manuscript.

## 2.2 | Polynomial reduced-order model

A data-driven dynamical system is used in the current wakeROM and is sought through a polynomial expansion of permutations of the POD coefficients. In essence, the method seeks a set of parameters that relate the POD coefficients to their respective time derivatives through a least-squares minimization, as proposed by Perret et al.<sup>26</sup> The dynamical system is defined in analogy to the Galerkin-POD structure, where parameters  $D_i$ ,  $L_{ij}$ ,  $Q_{ijk}$ , and  $C_{ijkl}$ , imply constant, linear, quadratic, and cubic mode interactions, respectively. The POD basis is truncated to  $N_r$  modes, and the coefficients are combined as

$$\frac{da_i}{dt} = D_i + \sum_{j=1}^{N_r} L_{ij} a_j + \sum_{j,k=1}^{N_r} Q_{ijk} a_j a_k + \sum_{j,k,l=1}^{N_r} C_{ijkl} a_j a_k a_l. \quad (7)$$

The parameters above are sought for the time derivative of each POD coefficient,  $da_i/dt$ , individually. Each index spans the POD mode space retained for flow description, on the interval  $i, j, k, l \in [1, N_r]$ . The polynomial combinations of the coefficients are reorganized as a vector  $\mathbf{A} = [1, a_j(t), a_j(t)a_k(t), a_j(t)a_k(t)a_l(t)]$  and the unknown parameters as  $\mathbf{X}_i = [D_i, L_{ij}, Q_{ijk}, C_{ijkl}]^T$ . Thus, the dynamical system can be more concisely written<sup>35</sup> as

$$\frac{da_i}{dt} = \mathbf{A}^T \mathbf{X}_i. \quad (8)$$

Error between the known time derivatives of the coefficients calculated from the POD and the fit provided by the parameters is expressed as

$$\chi^2 = \sum_{p=1}^N \left[ \frac{da_i}{dt} - \sum_{k=1}^N \mathbf{A}^T \mathbf{X}_i \right]^2. \quad (9)$$

Minimization is accomplished numerically by  $\chi^2 = \|\mathbf{AX} - \mathbf{B}\|^2$ , where  $\mathbf{B}$  contains the  $N$  samples of  $da_i/dt$ .

The coupled set of ordinary differential equations (ODEs) in Equation 7 does not use the POD modes to determine the behavior of the system; rather, the dynamics of the system are derived exclusively through the coefficients. A key advantage of this approach is the option to include higher-order (cubic or even quartic) terms in the description of the dynamical system. Higher-order terms are known to add complexity to the system without introducing instability.<sup>17,24,26</sup> Strict data requirements (ie, simultaneous realizations of  $a_i$  and  $da_i/dt$ ) can be a challenge for many experimental methods, although high-fidelity computational approaches (direct numerical and large eddy simulation) are capable of sufficient temporal resolution.

Solving the ODEs in Equation 7 yields a time series of coefficients predicting the relative intensities of each of the constituent modes in the ROM. Below, products of the ROM are denoted with a caret (^). The least-squares fit of the time derivatives of the POD coefficients is written  $\hat{da}_i/dt$ , the mode coefficients from the ROM are denoted by  $\hat{a}_i$ , and are function of a new vector of time values  $\hat{t}$ . The time resolution of  $\hat{a}_i(\hat{t})$  is related to the error tolerance of the numerical ODE solver and the number of modes in the system.<sup>26,33</sup>

Tikhonov regularization is undertaken by modifying the minimization above to fit the form,

$$\min(|\mathbf{AX} - \mathbf{B}|^2 - \rho^2 |\mathbf{L}(\mathbf{X} - \mathbf{X}_0)|^2), \quad (10)$$

where the second term in the minimization provides an additional constraint on the vector of parameters being sought,  $\mathbf{X}$ . In Equation 10, the regularization parameter is denoted as  $\rho$ , a discrete approximation matrix of a differential operator is introduced as  $\mathbf{L}$ , and an initial estimate of vector of parameters is considered as  $\mathbf{X}_0$ . The corner of the characteristic L-shaped curve corresponds to a fair balance between the 2 norms and is detected to obtain  $\rho$ . When no initial estimate is supplied or desired in the regularization,  $\mathbf{X}_0 = 0$ . The discrete differential operator is varied, taking  $\mathbf{L}$  as the identity matrix ( $\mathbf{I}$ ), a first-order difference matrix (FOD) or a second-order difference matrix (SOD). Higher-order difference operators are used to test the effects of smoothing in the regularization process.<sup>35</sup> In cases when  $\mathbf{L} \neq \mathbf{I}$ , the generalized singular value decomposition is implemented. Interested readers are referred to the "regularization tools" documentation<sup>41</sup> for more details.

## 3 | LARGE EDDY SIMULATION OF A WIND TURBINE

The data used in the following work rely on the LES code introduced in Sharma et al, which integrates the nondimensional, incompressible, and filtered Navier-Stokes momentum equations together with the continuity equation. The reader is referred to the works by previous studies<sup>4,42</sup> for a complete description of the LES framework and simulation details. The equations are implemented using a rotational form to assure conservation of energy and mass of the inertial terms.<sup>43</sup> The effects of temperature were removed from the current simulation, decoupling the temperature and velocity fields and forcing neutral atmospheric stratification. The flow is forced by a constant pressure gradient boundary condition to ensure the flow remains perpendicular to the wind turbine rotor.

$$\frac{\partial \tilde{u}_i}{\partial x_i} = 0, \quad (11)$$

$$\frac{\partial \tilde{u}_i}{\partial t} + \tilde{u}_j \left( \frac{\partial \tilde{u}_i}{\partial x_j} - \frac{\partial \tilde{u}_j}{\partial x_i} \right) = -\frac{1}{\rho} \frac{\partial p^*}{\partial x_i} - \frac{\partial \tilde{\tau}_{ij}}{\partial x_j} + f_i. \quad (12)$$

In Equations 11 and 12, a tilde ( $\tilde{\cdot}$ ) indicates an instantaneous quantity resolved above the LES filtering operation at the grid-size  $\Delta$ . The term  $\tilde{\tau}_{ij}$  represents the deviatoric part of the momentum subgrid stress term, which is modeled using the Lagrangian scale-dependent model of Bou-Zeid.<sup>44</sup> The filtered pressure term has been modified ( $p^*$ ) to include the trace of the subgrid stress tensor ( $\bar{p}/\rho + \tilde{\tau}_{kk}/3$ ). A forcing term  $f_i$  represents the momentum sink induced by the wind turbine that includes both axial and tangential components. In the simulation, the body force per unit volume  $f_i$  is modeled using the actuator-disc with rotation.<sup>45</sup>

Numerical discretization of the equations follows that used by Moeng<sup>46</sup> and Albertson.<sup>47</sup> The LES analyzed herein models a pseudospectral approach where a staggered-grid is used. Fourier discretization is used in the streamwise and spanwise directions, hence imposing periodic boundary conditions. The top boundary has zero-flux and zero-shear boundary conditions such that the vertical velocity and the gradients of the horizontal velocities are equal to zero. The lower surface has a no-slip condition, and because of the staggered grid, an equivalent surface shear stress is imposed at the first grid point for the horizontal velocities parameterized from the traditional log-law.

The LES analyzed here assesses a single wind turbine operating in the atmospheric boundary layer. Boundary effects, arising from a finite computational domain and periodic boundary conditions, are mitigated by ensuring that the domain is sufficiently large. This allows for the wake of the wind turbine to fully recover before reaching the outlet. The simulation domain consists of  $n_x = 512$ ,  $n_y = 128$ , and  $n_z = 384$  nodes in the streamwise, spanwise, and wall-normal directions, respectively. In physical dimensions, the simulation space occupies  $L_x = 12.3$ ,  $L_y = 1$ , and  $L_z = 1.5$  km. The numerical domain is shown in the schematic in Figure 1. With periodic boundary conditions, the simulation effectively guarantees the isolation of the wind turbine, as the flow develops for approximately  $S_x = 120D$  and  $S_z = 1.5D$  in the streamwise and spanwise directions before encountering the turbine again. The time resolution of the analyzed data is  $\Delta t = 2$  seconds. At measurement frequency, velocity fields remain highly correlated, and time derivatives can be accurately computed with reduced-order schemes.

The following analysis focuses on the wake of the wind turbine in the LES data; a subdomain of the simulation is extracted detailing the wake only. Figure 1 shows the wake subdomain as a volume inside the full LES domain. The figure shows a scaled wind turbine with blades and a rotor for context only; the LES uses an actuator disc approach, and the mast and blades of a wind turbine are not included in the simulation. The rotor disc spans  $5 \times 13$  grid points in the transverse and wall-normal directions, respectively. This grid resolution is considered sufficient to reproduce turbulence in the wind turbine wake.<sup>45</sup> A low-order dynamical system is developed below characterizing turbulence for the subdomain containing the wake. Table 1 summarizes key values from the subdomain of the LES used in the following analysis.

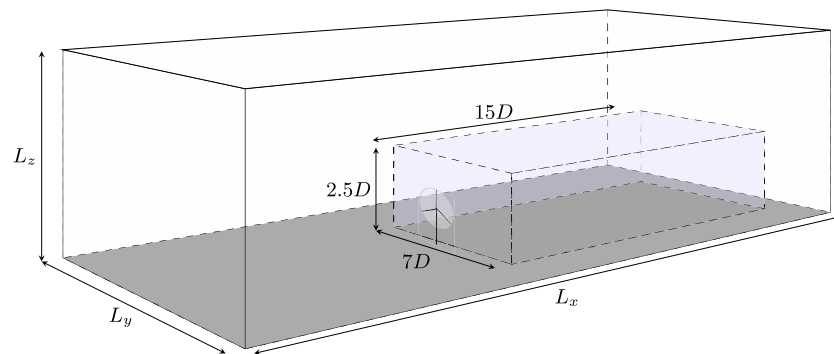


**FIGURE 1** Demonstration of the spatial domain used in the wind turbine large eddy simulation. Inner volume represents the subdomain analyzed in the present work. The light gray circle indicates the area of the actuator disc representing the wind turbine rotor [Colour figure can be viewed at [wileyonlinelibrary.com](http://wileyonlinelibrary.com)]

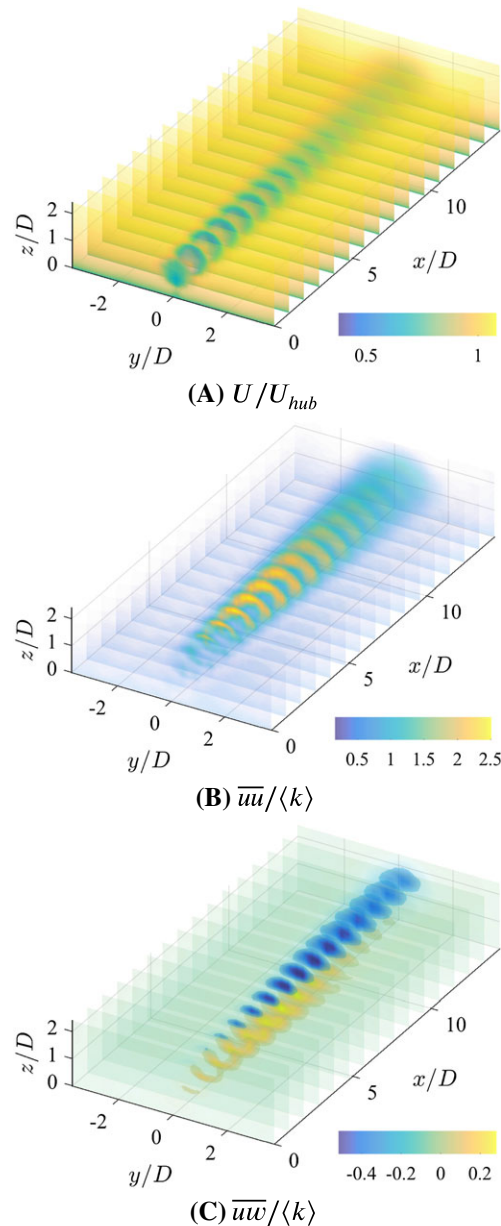
**TABLE 1** Details for the subdomain of the large eddy simulation domain extracted for the reduced-order model

$L_x$	1.6 km	$n_x$	64	$\Delta x$	24.5 m	rotor diameter, $D$	100 m
$L_y$	0.25 km	$n_y$	32	$\Delta y$	7.8 m	surface roughness, $z_0$	$3 \times 10^{-4}$ m
$L_z$	0.78 km	$n_z$	32	$\Delta z$	24.5 m	hub-height TI, $\sigma_{u,\text{hub}}$	0.057
$T$	4000 s	$n_t$	2000	$\Delta t$	2 s	hub-height velocity $U_{\text{hub}}$	14.4 m/s

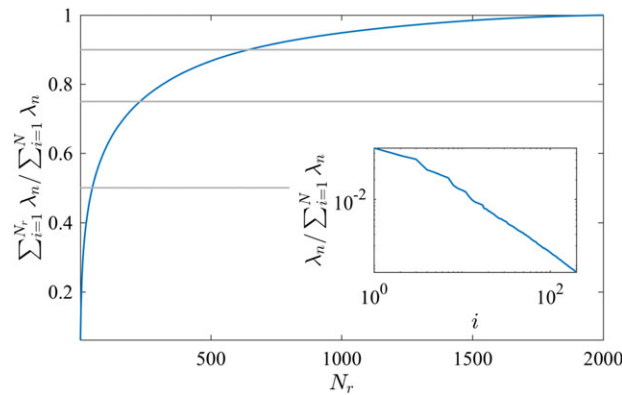
#### 4 | DATA-DRIVEN REDUCED-ORDER MODEL

Figure 2 shows selected statistical values from the wind turbine wake. The momentum deficit area of the wake is visualized in Figure 2A as the blue areas in the mean streamwise velocity. Because these data pertain to a single wind turbine in isolation, the momentum deficit in the wake extends farther downstream than one would expect for a wake within a large array of turbines, where higher levels of turbulence enhance mixing and wake recovery. The data in Figure 2 are ensemble averaged over the full range of the LES, ensuring statistical convergence of mean velocities. In each subfigure, transparency has been used to aid in visualization.

Normalized second-order wake statistics for selected components of the turbulence field are shown in Figure 2B,C. As a normalization scale, the turbulence kinetic energy is spatially averaged over the domain, denoted as  $\langle k \rangle$ . The streamwise Reynolds normal stress  $\overline{uu}/\langle k \rangle$  is positive by definition and shows peak values of approximately 2.75 trailing the rotor at the height of the top tip of the disc ( $z/D \approx 1.5$ ). Wake statistics for a single wind turbine in isolation evolve over greater distances in the streamwise direction than they would for a wind turbine in a large array.<sup>3</sup> Here, the peak values of  $\overline{uu}$  occur at  $x/D = 6$ . As the field evolves downstream, the contour plots show the growth of  $\overline{uu}$  trailing the swept area of the edge of the rotor disc, mainly above hub height.



**FIGURE 2** Mean velocity, streamwise normal Reynolds stress, and streamwise/wall-normal shear Reynolds stress in the wake of an isolated wind turbine [Colour figure can be viewed at [wileyonlinelibrary.com](http://wileyonlinelibrary.com)]



**FIGURE 3** Distribution of energy in the proper orthogonal decomposition mode basis according to eigenvalues  $\lambda_n$ . The cumulative fraction of eigenvalues is shown against thresholds corresponding 75%, and 90% of the integrated turbulence kinetic energy in the domain; normalized eigenvalues are shown in the inset figure, up to  $i = 47$ , corresponding to the 50% turbulence kinetic energy threshold [Colour figure can be viewed at [wileyonlinelibrary.com](http://wileyonlinelibrary.com)]

Turbulent shear stresses, represented by the off-diagonal terms of the Reynolds stress tensor, are smaller in magnitude than the Reynolds normal stresses. Flux of mean flow kinetic energy into the momentum deficit area of the wake is assisted by the shear stresses. However, for an isolated wind turbine, turbulent flux of mean flow kinetic energy is not a main contributor to the energy balance in the wake. Rather, shear stresses are expected to be most significant in higher-order statistics from the turbulence kinetic energy transport equation. The shear term  $\overline{uv}$  assists in vertical transport of mean flow kinetic energy. Positive values of  $\overline{uv}/\langle k \rangle$  occur below hub height and correspond to upward flux; negative values occur above hub height and correspond to flux downward from above the wake. Figure 2C indicates that there is a streamwise offset between the peak upward and downward fluxes of mean flow energy into the wake. The spanwise/wall-normal stress (not shown for brevity) is an order of magnitude smaller than the other components, as a result of the near-axisymmetry seen in the turbulence field.

In applying the proper orthogonal decomposition to the LES wake data, each snapshot is taken as a full volume of the fluctuating velocity field. The two-point cross-correlation tensor forming the kernel of the decomposition effectively accounts for the turbulence field characterized by the Reynolds stresses seen in Figure 2B,C. The cumulative summation of eigenvalues  $\lambda_n$ , shown in Figure 3, is used to establish the portion of energy represented by a truncated basis of POD modes. In the ROMs explored below, 47 modes are used, corresponding to 50.1% of the integrated TKE of the LES data. With 47 modes, the turbulence field may be described (as by Equation 5) to within approximately 18% according to the NRMSE outlined in Equation 6 and marks an acceptable compromise between basis truncation and accuracy. Eigenvalues of the POD from Equation 2 are shown in the inset of Figure 3, normalized by the integrated turbulence kinetic energy of the volume. Application of the POD to LES data shows slow accumulation of energy by mode due to periodicity in the simulation space. The nature of the subgrid filtering and periodic boundary conditions in the LES introduce homogeneity that slow the rate of convergence of  $\lambda_n$ .

Figure 4 reveals the vectorial magnitude of modes from the POD basis selected to demonstrate the increase in complexity with mode number. Color scale information is included for completeness, although it should be noted here that by convention, the modes do not carry physical units unless combined with their respective coefficients. The modes represent the spatially coherent structures in the wind turbine wake, ordered by their projection onto the turbulence field. The modes of lowest rank represent the largest and most energetic features of the wake. After the first few modes, it becomes increasingly difficult to associate each structure with features in the wake, although their contribution to the energy is defined by their associated eigenvalue. Similarity in structures exhibited by modes  $|\phi^{(1)}|$  through  $|\phi^{(8)}|$  (Figure 4A–D) arise from 2 sources: (1) snapshots are not statistically uncorrelated in time, and (2) the simulation domain of the LES is periodic. These effects cause some structures in the input snapshots to be overrepresented by the POD and appear in more than one mode. Mode pairing is commonly seen in POD applied to time-resolved data and do not affect the ability of the method to represent the turbulence field, but certainly slow the convergence of energy contained in the eigenvalues. Within the current data, mode pairing is evident between modes 2 and 3, modes 4 and 5, and modes 7 and 8. As the rank of the modes increases, mode pairing becomes less apparent, as structures become less coherent and represent more isotropic contributions to the overall turbulence field. Normalized eigenvalues in Figure 3 demonstrate mode pairing as “stair steps” in the distribution of energy. The dynamics of the input data described by the POD requires the contributions of relatively similar POD modes. For this reason, mode pairs are retained without a posteriori filtering (beyond the basis truncation) and are included in the reduced-order model. However, because mode pairs are statistically similar, individually, they do not contribute as much new information to the description of the turbulence field as unpaired modes. For this reason, convergence of energy is slower than in cases where mode pairing is not present.

The definition of the wakeROM requires that each mode coefficient interacts with the others in the truncated POD basis, often at several polynomial orders. Figure 5 shows the parameters coupling the dynamics of each mode ultimately used in the numerical solution according to Equation 7. The constant term is quite small ( $\mathcal{O} \sim 10^{-3}$ ) as each mode is zero-centered and shows no easily identified trend with mode index  $i$ . Linear mode



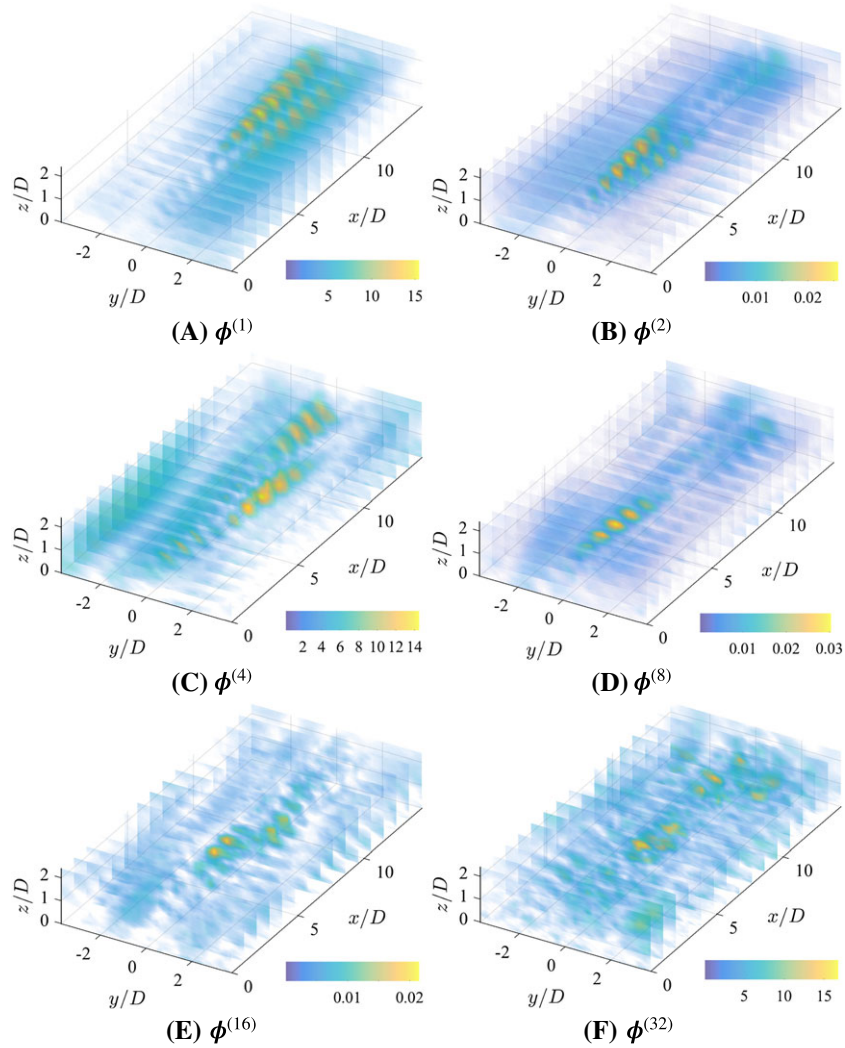


**FIGURE 4** Vector magnitude of selected proper orthogonal decomposition modes from the wind turbine wake [Colour figure can be viewed at [wileyonlinelibrary.com](http://wileyonlinelibrary.com)]

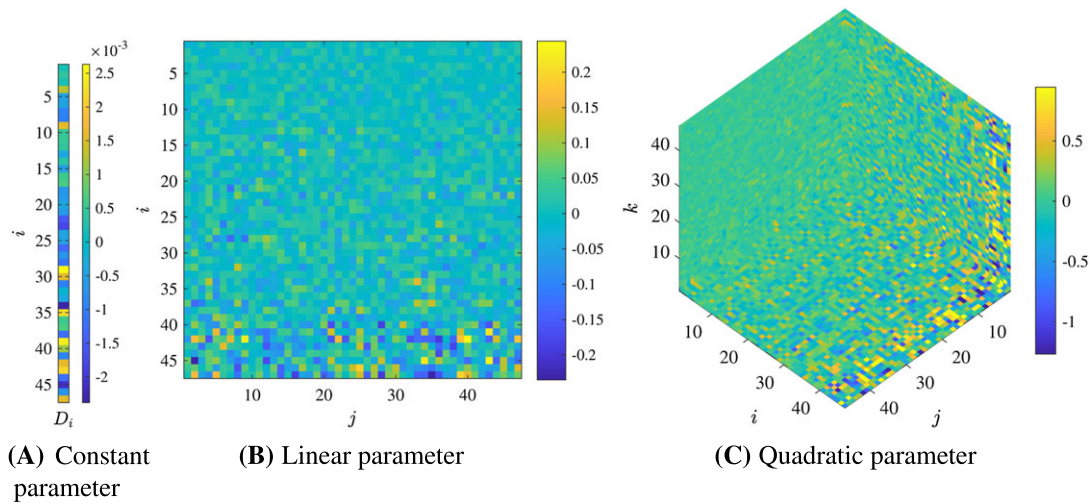


**FIGURE 5** A, Constant, B, linear, and C, quadratic parameters coupling the mode coefficients in the ROM. Cubic parameters are on the order of  $10^{-7}$  and are not included for brevity [Colour figure can be viewed at [wileyonlinelibrary.com](http://wileyonlinelibrary.com)]



interactions are shown in Figure 5B. In the Galerkin-POD method,  $L_{ij}$  describes the linear mode interactions arising from dissipation terms in the Navier-Stokes equations. The generally small values of  $L_{ij}$  ( $\mathcal{O} \sim 10^{-1}$ ) indicate that most of the linear interactions in the wakeROM are not dominant in the overall dynamics. Note that  $L_{ij}$  increases with the mode index along  $i$ , since most dissipation occurs at small, dissipative scales. Therefore, one may conclude that the linear interactions are more relevant to intermediate and high-order modes. Quadratic terms relate the dynamics arising from the nonlinear convection term in the traditional Galerkin projection. Here, they are derived through a least-squares fit rather than projection onto the Navier-Stokes equations but remain the dominant contributor ( $\mathcal{O} \sim 10^1$ ) to the wakeROM dynamics. The cubic terms are negligible when compared to the others in the wakeROM ( $\mathcal{O} \sim 10^{-7}$ ) and are not shown for brevity.

Physical significance of the parameters is taken here to be analogous to those in the Galerkin projection, explored at length by Noack et al.<sup>15</sup> Parameters are classified in terms of their contributions to components of the momentum balance suggested in the Navier-Stokes equations, including intermodal energy exchanges. The constant term in Figure 5A is small but non-null, indicating that some long-term instability must be expected in the dynamical system. Behavior of the quadratic parameter is less easily characterized, although it appears that extreme values of  $Q_{ijk}$  occur for high values of the index  $j$  and for an entire space of  $i$  and  $k$ , in Figure 5C. This trend indicates that the convective term in the Navier-Stokes equations is characterized by a wide range of mode interactions. This result is not surprising given that the nonlinear term in the Navier-Stokes equations, which is associated with  $Q_{ijk}$ , accounts for a wide range of turbulence scales.

The parameters discussed above are combined as in Equation 7 yielding a system of coupled ODEs that describe the evolution of the dynamical mode coefficients. Figure 6A shows the time derivative of selected POD mode coefficients from Equation 4 as time series in black. Coefficients shown in the figure correspond to the modes shown in Figure 4. Dynamics of each mode varies according to rank;  $da_i/dt$  shows larger, low-frequency features when  $i$  is low and much higher frequency oscillations with increasing mode number. Colored lines correspond to the coefficient derivatives

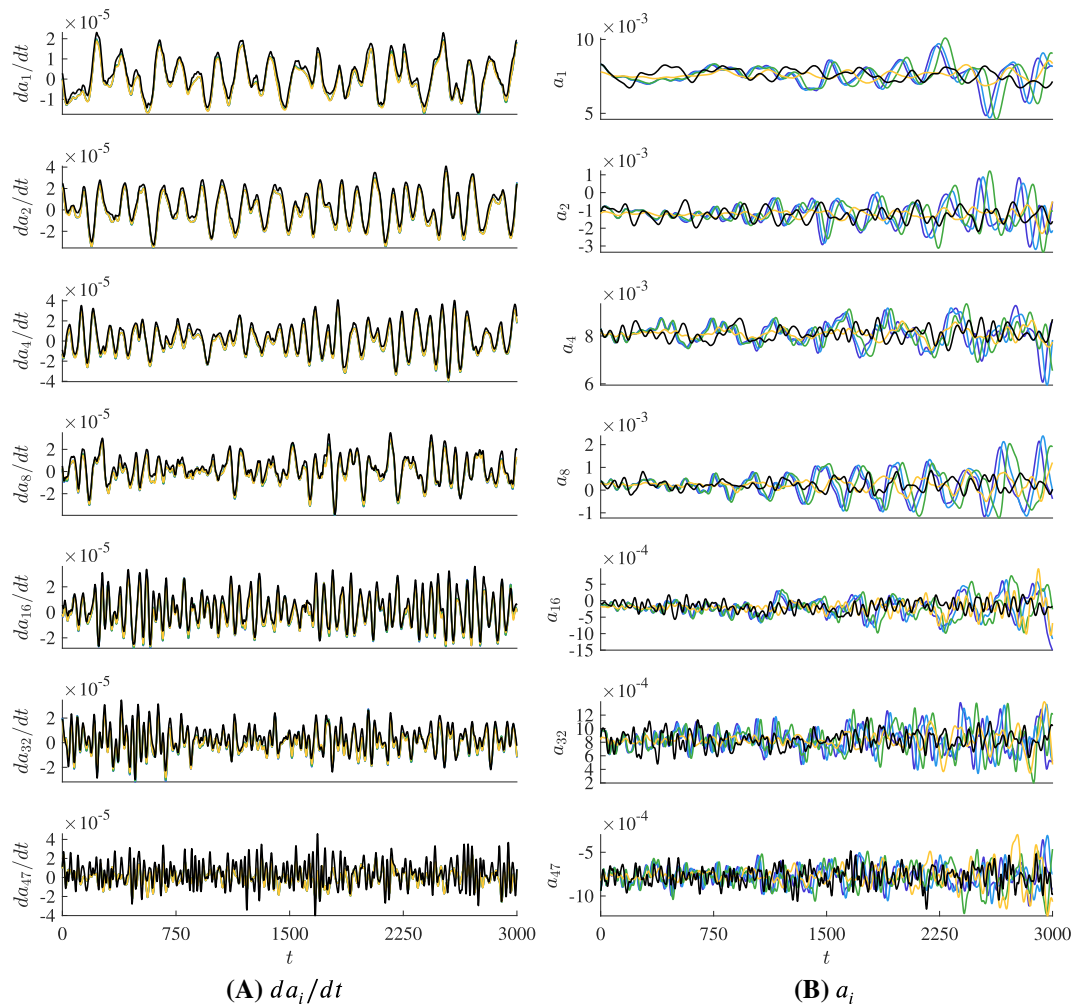


**FIGURE 6** Comparison between the time evolution (left subfigure) of selected proper orthogonal decomposition coefficients (black) and least-squares fit (dark blue). Solving the set of coupled ordinary differential equations in Equation 7 yields coefficients seen in right subfigure. Modeled mode coefficients from wakeROMs using Tikhonov regularization are shown in light blue ( $L = l$ ), green ( $L = \text{first-order difference}$ ), and yellow ( $L = \text{second-order difference}$ ) [Colour figure can be viewed at [wileyonlinelibrary.com](http://wileyonlinelibrary.com)]

from the wakeROM, using or forgoing the influence of Tikhonov regularization. Dark blue lines in Figure 6A result of the least-squares fit detailed in Equation 9 without any form of additional model regularization. The remaining time series in Figure 6A show the evolution of the mode coefficients with Tikhonov regularization fixing the differential operator as the identity matrix ( $L = I$ , light blue line), a first-order difference matrix ( $L = \text{FOD}$ , green lines), or a second-order difference matrix ( $L = \text{SOD}$ , yellow lines). Agreeing with previous applications of the technique,<sup>26,27</sup> the fit of  $d\hat{a}_i/dt$  is a good fit for  $da_i/dt$  for low rank modes, where low-frequency dynamics are dominant. Tikhonov regularization using the second-order differential operator ( $L = \text{SOD}$ ) removes variability from the system, suppressing the magnitude of  $a_i$  for low-ranking modes  $i \leq 8$ . For modes of rank  $i > 8$ , Tikhonov regularization with  $L = \text{SOD}$  produces estimates of  $a_i$  that grow unstable and have magnitudes greater than those of the other differential operators.

Solving the system of equations results in the modeled coefficients in Figure 6B. From the figure, estimated coefficients  $\hat{a}_i$  (blue) diverge from their respective values produced through back-projecting the POD modes onto the snapshot basis (black) regardless of the absence, presence, or form of model regularization. The system of ODEs described by Equation 7 is composed of 47 modes, corresponding to 50.1% of the integrated TKE. Increasing the number of modes used to describe the turbulence marginally increases the accuracy of the solutions  $\hat{a}_i$ , but the computational cost increases exponentially. Modeled coefficients are sought in a prescribed time interval, set here to match the span of the training data, and require initial conditions, taken as the first values of the POD coefficients  $a_i(t = 0)$ . Modeled coefficients match their respective values from the POD for a short range beyond their initial conditions, but take on different trajectories as error accumulates from numerical solution of the ODEs and in the least-squares fits of their respective time derivatives. While the trajectories of  $\hat{a}_i$  differ from  $a_i$ , Figure 6B demonstrates that each modeled coefficient exhibits dynamics of similar amplitude and frequency range as their respective match from the POD. Resolution in time of the modeled coefficients is determined by the error tolerances allowed in the numerical integration of Equation 7. Including a greater number of modes in the ROM increases their ability to match the trajectories of  $a_i$ , but require significantly more computing power and time to resolve. Regardless of the number of modes used in the ROM, the system of  $\hat{a}_i$  will eventually diverge and grow unstable given a sufficiently long integration time.

Long-term instability is expected in the numerical solution of the system of ODEs defining the present ROM, and the trajectories of the modeled mode coefficients are sensitive to their initial conditions. Divergence is most evident for  $a_1$  and  $a_{16}$  in Figure 6B, where the modeled coefficients rapidly take on values that differ from the known values of  $a_i$ , become unstable, and will eventually grow without bound. Using a higher-order differential operator  $L = \text{FOD}$  or  $L = \text{SOD}$  (green and yellow lines, respectively) stabilizes these modes and delays the divergence of these mode coefficients. However, even under the influence of Tikhonov regularization, the modeled coefficients  $\hat{a}_i$  do not match the POD mode coefficients (in black) and thus do not reflect incoming flow events, even if they remain stable. The value of a ROM that can accept information regarding inflow conditions cannot be overstated for wind energy and further underpins the need for additional system inputs. Any means of recalibrating or reinitializing the ROM must respect the dynamics delineated by the system of ODEs and inform the system of incoming flow dynamics if the reduced-order model is to be used in a predictive sense. The effective velocity seen by the rotor disc, defined by Equation 13, offers an intuitive signal to characterize incoming flow conditions.

Disparity between the known coefficients and their respective trajectories produced by the wakeROM is quantified with a normalized root-mean-square error given by Equation 6.  $\text{NRMSE}(\hat{a}_i)$  between each POD mode coefficient and its counterpart from the wakeROM is shown in Figure 7. From the figure, it is evident that Tikhonov regularization is able to improve the system moderately when using the identity matrix or the first-order differential operator  $L = \text{FOD}$ . Figure 7 shows that for modes  $i \leq 8$ ,  $L = \text{SOD}$  produces accurate estimates of the mode coefficients. However, for higher ranking modes, the wakeROM estimate with  $L = \text{SOD}$  produces coefficients that grow unstable, seen most clearly in  $\hat{a}_{16}$ ,  $\hat{a}_{32}$ , and  $\hat{a}_{47}$ . The total error associated with each version of the wakeROM (for the span of all coefficients as opposed from the NRMSE by mode) is 27.1% (without regularization), 27.4% (with  $L = I$ ), 25.2% (with  $L = \text{FOD}$ ), and 45.4% (with  $L = \text{SOD}$ ). The wakeROM with Tikhonov regularization and  $L = \text{FOD}$  exhibits the lowest NRMSE; hence, the other versions are not considered in the remaining analysis.

An input signal is used to periodically refresh the initial conditions for the wakeROM, shown in the flowchart in Figure 8. Process blocks are shown as diamonds and include decomposition into modes, tuning initial conditions from transfer functions, calibration of the reduced-order dynamical system, and reconstruction of the turbulent field in the wake. Inputs are shown as rectangles and include the statistical record of the wake, taken

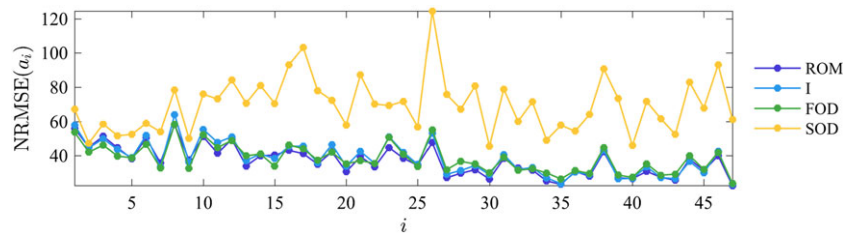


**FIGURE 7** Normalized root-mean-square error (NRMSE) between proper orthogonal decomposition mode coefficients and their respective wakeROM equivalents from the wakeROM without regularization (dark blue) and those using Tikhonov regularization in light blue ( $L = I$ ), green ( $L = \text{first-order difference [FOD]}$ ), and yellow ( $L = \text{second-order difference [SOD]}$ ) [Colour figure can be viewed at [wileyonlinelibrary.com](http://wileyonlinelibrary.com)]

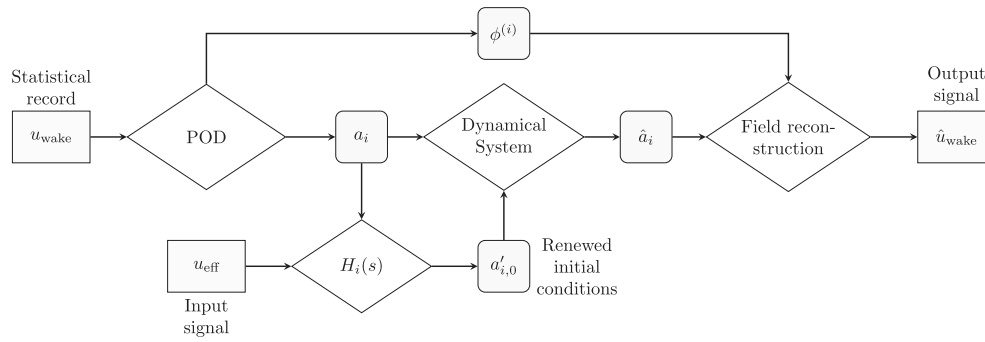


**FIGURE 8** Work flow demonstrating the input/output map of the dynamical system with periodic recalibration from the effective inflow velocity. POD, proper orthogonal decomposition

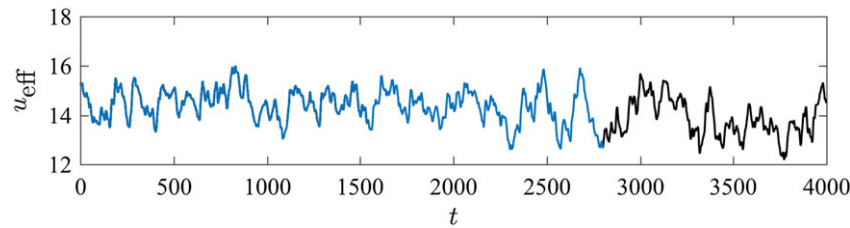


**FIGURE 9** Effective inflow velocity. Training data shown in blue; validation data shown in black [Colour figure can be viewed at wileyonlinelibrary.com]

here as the LES data, the effective inflow velocity used as the “input signal,” and the output is the modeled wake flow  $\hat{u}_{wake}$ . Intermediate variables are shown in squares with rounded corners and include the POD modes ( $\phi^{(i)}$ ) and coefficients ( $a_i$ ), the renewed initial conditions ( $a'_{i,0}$ ), as well as the modeled coefficients ( $\hat{a}_i$ ).

It is understood from previous work<sup>27</sup> that coefficients predicted by the ROM will diverge from those of the POD in long solution times. To ensure that the modeled wake reflects incoming turbulence, the wakeROM is periodically halted and reinitialized with new initial conditions supplied by relating the effective inflow velocity to the known coefficient values. Effective inflow velocity is calculated by integrating the instantaneous streamwise velocity over the swept area of the rotor immediately upstream of the turbine, shown as a gray circle in Figure 1, defined as,

$$u_{eff}(t) = \int_{A_{rotor}} \tilde{u}(t) dA. \quad (13)$$

Incoming flow information is provided to the wakeROM by relating  $u_{eff}$  to the POD mode coefficients  $a_i$  through a system of open-loop transfer functions  $H_i(s)$ . Each transfer function is tuned to maximize the fit to its respective mode coefficient by varying the number of poles and zeros, up to a maximum of 15 each; a time delay between input and output signals is sought as an addition fit parameter. For the sake of brevity, the transfer functions are presented without exhaustive supporting detail and are mainly intended to demonstrate the need for some means of relating the wakeROM to incoming flow information. A more complete discussion of the components of the wakeROM is outlined in Section 5.

Figure 9 shows  $u_{eff}(t)$  separated into 2 ranges; the portion of the signal shown in blue indicates the range over which  $u_{eff}$  was compared to  $a_i$  to define transfer functions, and the section in black is reserved as validation data. The inflow velocity  $u_{eff}$  is commonly used in the calculation of the fluid power available to the turbine. For calculation of the transfer functions,  $u_{eff}$  is normalized to vary over the interval [0,1]. The effective inflow velocity signal is compared to POD mode coefficients over the same time interval that have been similarly normalized. Transfer functions are calculated relating the inflow velocity signal to the POD coefficients in the wake optimizing the number and magnitudes of poles and zeros for best fit between  $u_{eff}$  and  $a_i$ .

Open-loop transfer functions are used to estimate new initial conditions for the dynamical system of the wake corresponding to the atmospheric flow interacting with the wind turbine rotor. Optimized transfer functions are limited to a maximum of 15 poles and 14 zero locations, and the NRMSE of the fit ranges between 4.57% for  $a_2$  and 45.6% for mode  $a_{47}$ . During the calculation of the transfer functions, both  $u_{eff}$  and  $a_i$  are renormalized to scale between 0 and 1. Renormalization speeds the calculation of the transfer functions by saving the algorithm from having to seek extra fit parameters. After calculation, the transfer functions,  $u_{eff}$ , and  $a_i$  are all scaled back to their original ranges. Table 2 shows details of the selected transfer functions used in the recalibration process.

Periodically refreshing the system with new initial conditions forces the solution to reflect the influence of the flow field incident to the rotor, within the error bounds of the transfer functions and dynamical system. However, once reinitialized, the dynamical model is again free to take on

**TABLE 2** Details for transfer functions relating  $u_{\text{eff}}$  to the training data of each POD mode coefficient. Modes shown in the table correspond those discussed above and shown in Figures 4 and 11

Mode	1	2	4	8	16	32
Poles	14	15	15	15	15	14
Zeros	7	13	11	8	14	13
Time delay, s	50	40	4	58	0	16
NRMSE, %	6.35	4.57	9.22	12.36	19.64	22.4

Abbreviations: NRMSE; normalized root-mean-square error; POD, proper orthogonal decomposition.

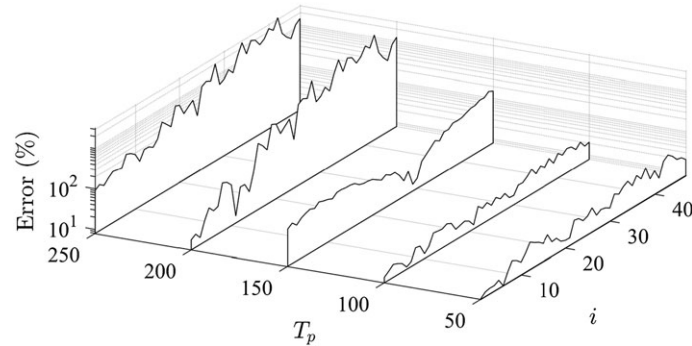


**FIGURE 10** Fit between coefficients predicted by dynamical model and their respective values from proper orthogonal decomposition. Coefficients for each mode  $i$  are tested for a range of time periods  $T_p$  (in seconds)

its own trajectory that may deviate from that of the physical system. Thus, the degree of fit between the model and the true coefficient space is necessarily a function of the time interval between periodic reinitializations. Large time intervals between the supply of fresh initial conditions allow the modeled system to deviate further from the validation data, taken as the POD coefficients.

The range of reinitialization time intervals tested for each mode coefficient in Figure 10 suggests that as the period between renewed initial conditions  $T_p$  is reduced, the error is minimized. On the contrary, large time periods between recalibration allow the system to deviate far enough that the transfer functions are not able to supply the appropriate corrections. In the case where  $T_p = 250$  seconds, the error grows toward  $\mathcal{O}(10^3)$ , indicating that the transfer functions are not able to correct for the deviation in the wakeROM.

As recommended by the fit analysis in Figure 11, a short time period between reinitialization is selected for the model; transfer functions are able to supply the necessary information to the ROM to inform the model of the inflow, given a sufficiently short reinitialization time scale. Modeled coefficients  $\hat{a}_i$  exhibit discontinuities that arise from halting and restarting the solution to the dynamical system. Discontinuities are difficult to detect for low mode numbers but become more obvious for intermediate and high-rank modes. Given the effective inflow mean velocity at hub height of  $U_{\text{hub}} = 14.4$  m/s, the maximum distance into the wake that the flow could be convected over the prediction horizon  $T_p = 50$  seconds is approximately  $7.5D$ , which is on the scale of common spacing of turbines within an array. At this reinitialization schedule, the model is updated on the scale of time for flow information to evolve from one turbine to the next in an array setting. While the wake of the isolated wind turbine analyzed here spans closer to  $15D$ , the current results with a 50-second reinitialization horizon is promising for an analogous reduced-order model for a wind turbine array.

Sudden changes seen in modeled mode coefficients propagate through to fluctuating velocity snapshots in the wake as abrupt shifts in the velocity fields in time. The time series of velocity output by wakeROM are compared in Figure 12 at selected points in the wake. Each of the figures corresponds to the time series of fluctuating velocity aligned with the center of the rotor disc ( $(y/D, z/D) = (0, 1)$  at locations  $x/D \in [0, 5, 10, 15]$  into the wake). Velocity signals produced by the ROM (green) are able to capture large-scale behavior, but like the POD, exhibit low-pass filtering as compared to the LES data. Discontinuities present in the modeled coefficients are seen in the velocity signals as well. Filtering is mitigated by adjusting the point of truncation of the POD mode basis accounting for both spatial filtering through the modes ( $\phi^{(i)}$ ) and temporal filtering through the associated coefficients ( $a_i$ ). For comparison, Figure 12 shows the time series predicted by the POD in blue. The overlap of the wakeROM and the POD coefficients confirms that the dynamical system introduces minimal filtering of the predicted velocity fields beyond that of the POD.

Discontinuities seen in the time series above (highlighted in Figure 13) are not distinctly visible after ensemble averaging to reach the Reynolds stresses shown in Figure 14. In ensemble, turbulence statistics in the modeled wake closely reflects features demonstrated in the statistics calculated directly from the LES. Terms from the modeled turbulent stress tensor are shown in Figure 14. The color scale of each subfigure is fixed to that of the original statistical values of each stress for ease of comparison.

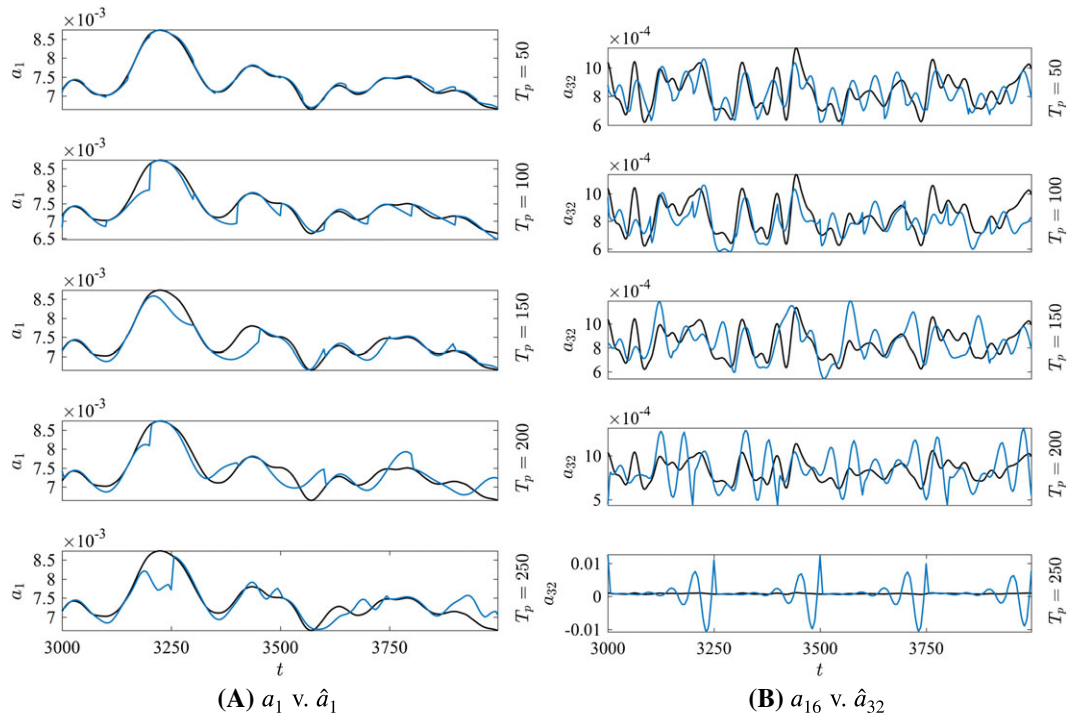


**FIGURE 11** Comparison of validation data (black) to predictions of the regularized wakeROM (blue). In each subfigure, from top are reinitialization horizons of  $T_p \in [50, 100, 150, 200, 250]$  seconds. Coefficients of only 2 modes ( $a_1$  and  $a_{32}$ ) are shown for brevity [Colour figure can be viewed at [wileyonlinelibrary.com](http://wileyonlinelibrary.com)]

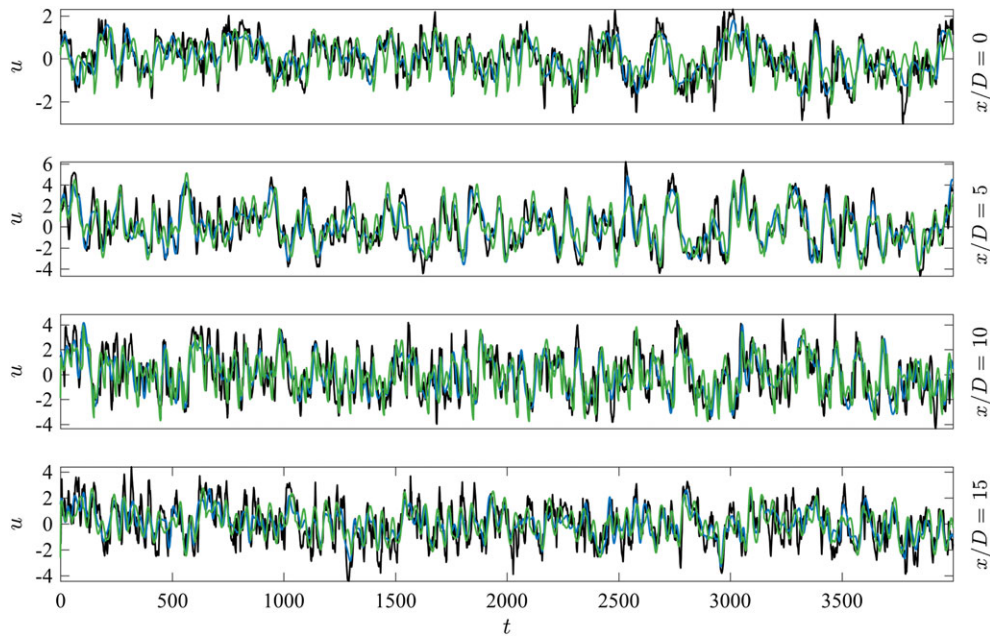


**FIGURE 12** Comparison of velocity signals at locations downstream of the wind turbine. Green lines are  $\hat{u}_{\text{wake}}$  integrated over the swept area of the rotor, black lines are validation data from the large eddy simulation, and blue lines are produced with proper orthogonal decomposition. Fluctuating velocity signals correspond to points aligned with the center of the rotor disc ( $(y/D, z/D) = (0, 1)$ ) at locations  $x/D \in [0, 5, 10, 15]$  downstream of the rotor disc [Colour figure can be viewed at [wileyonlinelibrary.com](http://wileyonlinelibrary.com)]

The modeled streamwise normal stress  $\hat{u}\hat{u}$  demonstrates the same characteristic feature evolving with  $x/D$  trailing the top tip of the rotor disc. It is expected that the modeled stresses will demonstrate reduced magnitudes compared to those arising from the original statistics. The difference in magnitudes is attributed to truncating the basis of modes to  $N_r$  in the model and reconstruction; only 47 of 2000 modes are used and account for 50.1% of the total turbulence kinetic energy of the wake.



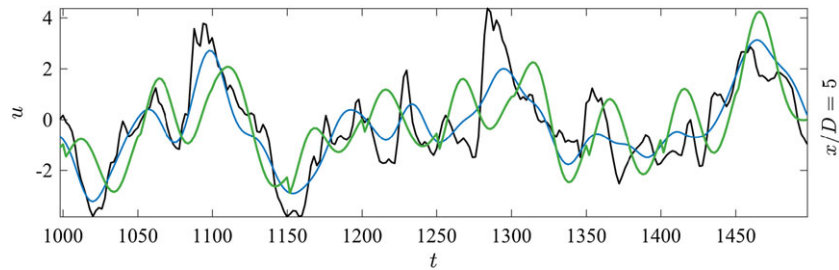


**FIGURE 13** Detail comparison of reconstructed fluctuating velocity signal in the wake highlighting discontinuities that arise from the reinitialization process (green line, every 50 seconds from  $t = [1000, 1500]$ ) [Colour figure can be viewed at [wileyonlinelibrary.com](http://wileyonlinelibrary.com)]

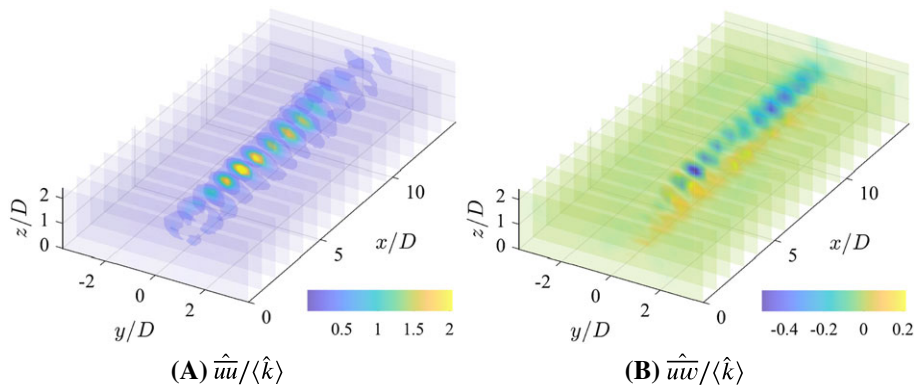


**FIGURE 14** Reynolds stresses produced by the wakeROM using 32 proper orthogonal decomposition modes, Tikhonov regularization with a second-order differential operator ( $L = \text{SOD}$ ), and iterative reinitialization with open-loop transfer functions. Equivalent Reynolds stresses from the large eddy simulation are shown in Figure 2, for comparison [Colour figure can be viewed at [wileyonlinelibrary.com](http://wileyonlinelibrary.com)]

## 5 | DISCUSSION ON GENERALIZING THE WAKEROM

The wakeROM detailed above uses one particular combination of methods and algorithms (of many possible options) to produce mode coefficients that reflect incoming flow events and provide a dynamic estimate of the turbulence in a wind turbine wake. Within the approach explored here, several of the model inputs and processes require further exploration or development to reflect a general wake model that can be used in plant optimization. Figure 15 shows a generalized version of the workflow used in the current wakeROM, highlighting areas for further exploration.

While the wakeROM developed in the current work represents significant progress toward a broadly applicable modeling tool, there remain several points that require additional investigation. The first and most significant consideration in making a generalized ROM is ensuring that the resultant model reflects the full range of operating conditions that a wind turbine is likely to encounter. The statistical record (Figure 15, top left) must necessarily be expanded from the limited data set used to train the model here to one that includes the effects of terrain, thermal stratification and atmospheric stability due to diurnal and seasonal cycles, and interaction of wakes within an array. Offering the wakeROM a more complete range of training data presents a challenge in terms of both data collection and decomposition.

Proper orthogonal decomposition was selected to identify and isolate the dynamics of interest from the statistical record. Snapshot POD as used here is an intuitive means of identifying the optimal modal basis with respect to kinetic energy, which is advantageous in terms of representing the important dynamics of a wind turbine wake. To date, the POD remains unproven in its ability to effectively recover transient phenomena such as dynamic wake meandering, although some notable development has been undertaken to these ends.<sup>13</sup> Additionally, further development will be required to make a POD-based dynamical system effective over the full parameter space of wind turbine operating conditions. Parameter-varying reduced-order models were explored for wind turbine wakes in Annoni and Seiler<sup>48</sup> and shows promise for generalizing the wakeROM constructed above. Many alternate means of decomposition have been applied to turbulent velocity data such as the dynamical mode decomposition,<sup>49</sup> balanced POD,<sup>50</sup> and empirical mode decomposition<sup>51</sup> to name a few.

Another means of modifying the proposed wakeROM without changing the overall workflow comes through testing additional dynamical system models. The dynamical system approach pursued here explores a data-driven method interrelating the dynamic POD mode coefficients with a set of parameters of increasing polynomial order, but many other dynamical systems are potentially suitable for the task of wake modeling. There exists a wide range of other data-driven (black-box or gray-box) models that could offer means of stabilizing or otherwise extending the capabilities of the current ROM.<sup>25</sup> Among the most favorable and well-tested reduced-order modeling approaches in turbulence is the traditional POD-Galerkin projection, which reconciles the governing behavior law with the modal basis directly. The low-order dynamical system model using polynomial



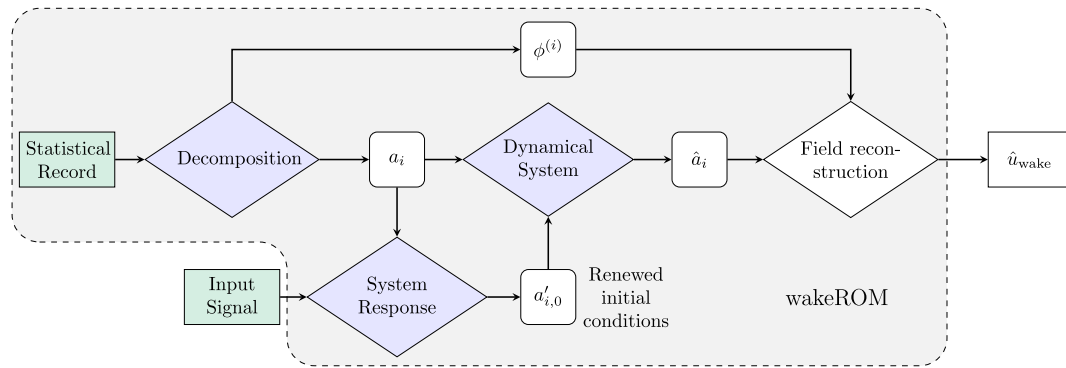


**FIGURE 15** Generalized workflow used in the current reduced-order modeling. Input and process blocks requiring additional development are shown in green and blue, respectively. Regardless of algorithms selected, the current wakeROM workflow, shown in gray, can be deployed equivalently for wind plant modeling, control, and optimization [Colour figure can be viewed at [wileyonlinelibrary.com](https://onlinelibrary.wiley.com)]

coefficients shares the form of the arguably more physical Galerkin-POD method. However, being a data-driven approach, the current wakeROM benefits from being intuitive and efficient to calculate and does not rely on the strong closure assumptions often necessary to keep Galerkin models stable such as eddy viscosity and diffusion models.<sup>20,22,23,25</sup> Considering this additional cost along side the full range of operating conditions discussed above may require computational resources sufficient to defeat the purposes of reduced-order modeling at all.<sup>26</sup> Neural networks continue to gain attention in recent flow control and predictive modeling applications, and may offer an accurate and stable path toward wake modeling, give that a sufficiency of data may be provided to train the network.<sup>23,52</sup>

The final components of the above workflow that merit further investigation work together to offer the wakeROM information regarding incoming flow events. It is certain that the wakeROM outlined here will produce estimates of the turbulence field in a wind turbine wake that differ from observed events. Even if the model remains stable, the modeled wake turbulence will eventually diverge from the actual or observed wake due to a combination of factors. The most prevalent sources of error are that the ROM necessarily excludes dynamics from the system for the sake of computational efficiency and error accumulates in any numerical solution of differential equations, regardless of tolerances. Offering exogenous inputs to the system provides a means of tuning the wakeROM to reflect incoming flow events and opens a path toward defining feedback mechanisms, control strategies, and optimization.

The current work relates a single input signal, the effective inflow velocity  $u_{\text{eff}}$ , to the mode coefficients through a system of open-loop transfer functions. Calculating or estimating new initial conditions for the dynamical system can be done in many ways, ranging from transfer functions to autoregressive models to Kalman filtering<sup>53,54</sup> and state estimation techniques. In a practical application,  $u_{\text{eff}}$  may not be easily provided to the wakeROM for wind turbines, although recent work has proposed forward-facing LIDAR systems to provide just such an input for simulations and field application.<sup>42,55</sup> Alternatively, the effective inflow velocity could be estimated using power, pitch angle, and rotational speed along with some other models as in Bozkurt et al.<sup>56</sup> Currently, it is commonplace for modern wind turbines to be outfitted with a large range of sensors or monitoring instrumentation that provide supervisory control and data acquisition (SCADA) information and could easily be leveraged as inputs in the system<sup>57</sup> from Figure 15.

Low-dimensional models like the one proposed here represent a possible path for computationally efficient wake modeling reflective of incoming flow events that should lead ultimately to real-time control strategies for wind turbine wakes and optimized wind plant power production. The ability to tune the model to an incoming velocity signal means that the model could be iteratively linked in a wind plant setting, shown in Figure 16. In the modified flowchart, the entirety of the above modeling procedure is contained in the gray box, excluding only the input signal and the modeled wake. Connecting instances of the wakeROM together as suggested in Figure 16 also offers a direct means of providing feedback for optimization and control. In the figure, the wind turbine operating parameters describing the yaw angle of the rotor relative to the inflow ( $\theta$ ), the blade pitch ( $\beta$ ), and the loading in the nacelle ( $\Omega$ ) are proposed for feedback mechanisms. Other parameters, such as the atmospheric conditions, are less desirable mechanisms as they are not easily controlled or modified. Among the inputs offered to the wakeROM in the control network are estimates of the power produced by each wind turbine (denoted as  $WT_a$  and  $WT_b$ ). Real-time estimates of the power produced by each wind turbine are part of the SCADA information discussed above and should provide a means of reaching a dynamic optimization of the wind plant.

In addition to control and optimization, a generalized reduced-order model for a wind turbine wake will also be extremely important for the next generation of wind plant design tools. The complexity of wind turbine wake turbulence, wake interaction, and the large range of operating conditions seen by a wind plant make a priori estimates of new wind farms difficult to rely on. Combining the inherent complexity of the wake dynamics with the sensitivity of wind turbine micro-siting makes the iterative process of wind plant design optimization very expensive with conventional means.<sup>58-60</sup> Because the computational costs of high-fidelity models remain a significant hurdle, engineering and empirical models are still commonly used in wind plant design but fail to describe the dynamics that are now understood to contribute to poor plant performance and increased operations and

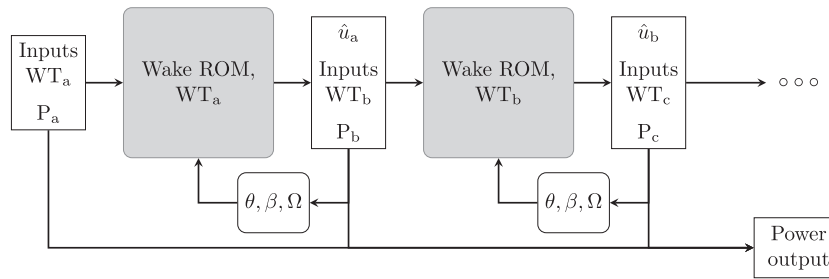


**FIGURE 16** Control network for wind plant modeling, control, and optimization connecting separate instances of a generalized wakeROM

maintenance costs. The ideal design tool then is one that is sufficiently complex to describe turbulent wind turbine wakes and efficient enough to be used iteratively for design optimization.

## 6 | CONCLUSIONS

Predictive models of wind turbine wakes are necessary for optimal design and operation of large wind turbine arrays, although the complex turbulent wake flows remain a challenge. Simulations such as the one analyzed above provide increasingly real physics with the necessary temporal and spatial resolution to determine loading conditions and dynamic evolution of the wake. However, the computational cost of LES prohibits the method from being applicable for continuous-time modeling or monitoring of wake flows. In many wind farms, monitoring of wind turbine wakes and operating conditions is difficult, if not prohibitively expensive. Modeling and prediction as in the scheme undertaken here present a possible path forward for diagnosing control schemes and monitoring techniques easily and uniquely adapted to wind turbines in the field.

Using high resolution data from LES simulations, the dominant features of the turbulence flow field are characterized using the proper orthogonal decomposition, optimal for describing the energy of the flow with the fewest modes. Low-dimensional models are generated combining the time series of mode coefficients through a least-squares error minimization of their time derivatives. The dynamic evolution of the mode coefficients is coupled to ordinary differential equations by way of polynomial coefficients up to cubic order. Solving the coupled set of ODEs results in predictions of mode coefficients that can then be used to reconstruct fluctuating velocity fields in the wind turbine wake. Predicted trajectories of the mode coefficients are sensitive to initial conditions, diverging from validation trajectories and ultimately becoming unstable. Residual errors, as a result of defining the coupling parameters of the ROM via least-squares minimization, propagate through to the ODEs and accumulate in their solution over time.

The dynamical wake model is trained to reflect the influence of the flow field incident to the wind turbine rotor. Incoming flow information is offered to the dynamical system through a series open-loop transfer functions that periodically supply refreshed initial conditions to the system. Validation data of the mode coefficients are compared to predicted values using recalibration at a variety of time intervals, showing that a nearly perfect fit is possible with sufficiently short prediction horizons. Transfer functions are optimized for their ability to match the time series of the POD coefficients during the training period, constrained only by a maximum of 15 poles. The recalibration method applied here is equally feasible for any dynamical system, provided an input signal is readily available to inform the time evolution of the mode coefficients.

Modeling and control using reduced-order dynamical systems as proposed here will require further development of the transfer functions used to supply refreshed initial conditions to the reduced-order model. The wakeROM will greatly benefit in future work from a thorough exploration into the range of possible inputs and processes that a turbine may experience in real operating conditions, including strong gusts or high inflow turbulence intensity. The control parameters will also need to be redefined for wind turbine wakes in large arrays, where wake dynamics, and thus the evolution of modes and coefficients will differ from those presented above.

## ACKNOWLEDGEMENTS

The authors would like to acknowledge the US National Science Foundation for supporting the above work (grant nos. NSF-ECCS-1032647 and NSF-CBET-1034581). In addition, Hamilton is grateful for support from National Science Foundation IGERT grant no. 0966376. Computing resources from the CPHC at the University of Utah were instrumental in the current work.

## ORCID

Nicholas Hamilton  <http://orcid.org/0000-0003-3462-341X>

## REFERENCES

1. Barthelmie RJ, Pryor SC, Frandsen ST, et al. Quantifying the impact of wind turbine wakes on power output at offshore wind farms. *J Atmos Oceanic Technol.* 2010;27(8):1302-1317.
2. Cal RB, Lebrón J, Castillo L, Kang HS, Meneveau C. Experimental study of the horizontally averaged flow structure in a model wind-turbine array boundary layer. *J Renewable Sustainable Energy.* 2010;2(1):013106.
3. Vermeer LJ, Sorensen JN, Crespo A. Wind turbine wake aerodynamics. *Prog Aerosp Sci.* 2003;39:457-510.
4. Calaf M, Meneveau C, Meyers J. Large eddy simulation study of fully developed wind-turbine array boundary layers. *Phys Fluids.* 2010;22(1):015110.
5. Hasselmann K. Pips and pops: The reduction of complex dynamical systems using principal interaction and oscillation patterns. *J Geophys Res Atmos* (1984-2012). 1988;93(D9):11015-11021.
6. Rempfer D. On low-dimensional Galerkin models for fluid flow. *Theor Comput Fluid Dyn.* 2000;14(2):75-88.
7. Lumley JL. The structure of inhomogeneous turbulent flows. *Atmos Turbul Radio Wave Propag.* 1967:166-178.
8. Sirovich L. Turbulence and the dynamics of coherent structures. *Q Appl Math.* 1987;45:561-571.
9. Saranyasoontorn K, Manuel L. Low-dimensional representations of inflow turbulence and wind turbine response using proper orthogonal decomposition. *J Sol Energy Eng.* 2005;127(4):553-562.
10. Hamilton N, Tutkun M, Cal RB. Wind turbine boundary layer arrays for cartesian and staggered configurations: part II, low-dimensional representations via the proper orthogonal decomposition. *Wind Energy.* 2015;18(2):297-315.
11. Hamilton N, Tutkun M, Cal RB. Low-order representations of the canonical wind turbine array boundary layer via double proper orthogonal decomposition. *Phys Fluids.* 2016;28(2):025103.
12. Andersen SJ, Sørensen JN, Mikkelsen R. Reduced order model of the inherent turbulence of wind turbine wakes inside an infinitely long row of turbines, *Journal of Physics Conference Series.* IOP Publishing; 2014;555(1):012005.
13. Bastine D, Witha B, Wächter M, Peinke J. POD analysis of a wind turbine wake in a turbulent atmospheric boundary layer, *Journal of Physics: Conference Series,* IOP Publishing; 2014;524(1):012153.
14. VerHulst C, Meneveau C. Large eddy simulation study of the kinetic energy entrainment by energetic turbulent flow structures in large wind farms. *Phys Fluids.* 2014;26(2):025113.
15. Noack BR, Afanasiev K, Morzynski M, Tadmor G, Thiele F. A hierarchy of low-dimensional models for the transient and post-transient cylinder wake. *J Fluid Mech.* 2003;497:335-363.
16. Aubry N, Holmes P, Lumley JL, Stone E. The dynamics of coherent structures in the wall region of a turbulent boundary layer. *J Fluid Mech.* 1988;192:115-173.
17. Braud C, Heitz D, Arroyo G, Perret L, Delville J, Bonnet J-P. Low-dimensional analysis, using POD, for two mixing layer-wake interactions. *Int J Heat Fluid Flow.* 2004;25(3):351-363.
18. Tadmor G, Lehmann O, Noack Bernd R, et al. Reduced-order models for closed-loop wake control. *Philosophical Transactions of the Royal Society of London A: Mathematical, Physical and Engineering Sciences.* 2011;369(1940):1513-1524.
19. Rowley Clarence W, Colonius T, Murray Richard M. Model reduction for compressible flows using POD and Galerkin projection. *Physica D Nonlinear Phenom.* 2004;189(1):115-129.
20. Öst J, Noack Bernd R, Krajnovic S, Barros D, Borée J. On the need for a nonlinear subscale turbulence term in POD models as exemplified for a high-Reynolds-number flow over an Ahmed body. *J Fluid Mech.* 2014;747:518-544.
21. Pastoor M, Henning L, Noack Bernd R, King R, Tadmor G. Feedback shear layer control for bluff body drag reduction. *J Fluid Mech.* 2008;608:161-196.
22. Podvin B. A proper-orthogonal-decomposition-based model for the wall layer of a turbulent channel flow. *Phys Fluids (1994-present).* 2009;21(1):015111.
23. Noack Bernd R, Morzynski M, Tadmor G. *Reduced-order Modelling for Flow Control*, Vol. 528: Springer Science & Business Media; 2011.
24. Favier J, Kourta A, Cordier L, Iollo A. Calibrated POD reduced-order models of massively separated flows in the perspective of their control. *American Society of Mechanical Engineers*; 2006:743-748.
25. Brunton S., Noack B.. Closed-loop turbulence control: progress and challenges. *Appl Mech Rev.* 2015;67(5):050801.
26. Perret L, Collin E, Delville J. Polynomial identification of POD based low-order dynamical system. *J Turbul.* 2006;7:N17.
27. Hamilton N, Tutkun M, Cal RB. Low-order dynamical system model of a fully developed turbulent channel flow. *Phys Fluids.* 2017;29(6):065107.
28. Polifke W. Black-box system identification for reduced order model construction. *Ann Nucl Energy.* 2014;67:109-128.
29. Sirisup S, Karniadakis GE, Xiu D, Kevrekidis IG. Equation-free/Galerkin-free POD-assisted computation of incompressible flows. *J Comput Phys.* 2005;207(2):568-587.
30. Romijn R, Özkan L, Weiland S, Ludlage J, Marquardt W. A grey-box modeling approach for the reduction of nonlinear systems. *J Process Control.* 2008;18(9):906-914.
31. Cordier L, Noack BR, Tissot G, et al. Identification strategies for model-based control. *Exp Fluids.* 2013;54(8):1580.
32. Couplet M, Basdevant C, Sagaut P. Calibrated reduced-order POD-Galerkin system for fluid flow modelling. *J Comput Phys.* 2005;207(1):192-220.
33. D'adamo J, Papadakis N, Mémín E, Artana G. Variational assimilation of pod low-order dynamical systems. *J Turbul.* 2007;8:N9.
34. Bergmann M, Cordier L. Optimal control of the cylinder wake in the laminar regime by trust-region methods and pod reduced-order models. *J Comput Phys.* 2008;227(16):7813-7840.
35. Cordier L, Majd E, Abou B, Favier J. Calibration of POD reduced-order models using Tikhonov regularization. *Int J Numer Methods Fluids.* 2010;63(2):269-296.

36. Kalashnikova I, Arunajatesan S, Barone MF, Bloemen Waanders BG, Fike JA. Reduced order modeling for prediction and control of large-scale systems. *SIAM J Matrix Anal Appl. SAND*. 2014;(2014-4693).
37. Benosman M, Borggaard J, Kramer B. Robust reduced-order model stabilization for partial differential equations based on Lyapunov theory and extremum seeking with application to the 3D boussinesq equations. *arXiv preprint arXiv:1604.04586*. 2016.
38. Golub GH, Hansen PC, O'Leary DP. Tikhonov regularization and total least squares. *SIAM J Matrix Anal Appl*. 1999;21(1):185-194.
39. Hamilton N, Kang H-S, Meneveau C, Cal RB. Statistical analysis of kinetic energy entrainment in a model wind turbine array boundary layer. *J Renewable Sustainable Energy*. 2012;4(6):063105-063105.
40. Hamilton N, Tutkun M, Cal RB. Anisotropic character of low-order turbulent flow descriptions through the proper orthogonal decomposition. *Phys Rev Fluids*. 2017;2(1):014601.
41. Hansen PC. Regularization tools: a Matlab package for analysis and solution of discrete ill-posed problems. *Numer Algorithms*. 1994;6(1):1-35.
42. Sharma V, Calaf M, Lehning M, Parlange MB. Time-adaptive wind turbine model for an LES framework. *Wind Energy*. 2016;19(5):939-952.
43. Orszag SA, Pao Y-H. Numerical computation of turbulent shear flows. *Adv. Geophys*. 18(1975):1974:225-236.
44. Bou-Zeid E, Meneveau C, Parlange M. A scale-dependent lagrangian dynamic model for large eddy simulation of complex turbulent flows. *Phys Fluids*. 2005;17(2):025105.
45. Wu Y-T, Porté-Agel F. Large-eddy simulation of wind-turbine wakes: evaluation of turbine parametrisations. *Boundary Layer Meteorol*. 2011;138(3):345-366.
46. Moeng C-H. A large-eddy-simulation model for the study of planetary boundary-layer turbulence. *J Atmos Sci*. 1984;41(13):2052-2062.
47. Albertson JD, Parlange MB. Natural integration of scalar fluxes from complex terrain. *Adv Water Res*. 1999;23(3):239-252.
48. Annoni J, Seiler P. A method to construct reduced-order parameter-varying models. *Int J Robust Nonlinear Control*. 2017;27(4):582-597.
49. Schmid PJ. Dynamic mode decomposition of numerical and experimental data. *J Fluid Mech*. 2010;656:5-28.
50. Willcox K, Peraire J. Balanced model reduction via the proper orthogonal decomposition. *AIAA J*. 2002;40(11):2323-2330.
51. Huang NE, Shen Z, Long SR, et al. The empirical mode decomposition and the Hilbert spectrum for nonlinear and non-stationary time series analysis. *Proceedings of the Royal Society of London A: mathematical, physical and engineering sciences*; 1998;454(1971):903-995.
52. Yuhong Z, Wenxin H. Application of artificial neural network to predict the friction factor of open channel flow. *Commun Nonlinear Sci Numer Simul*. 2009;14(5):2373-2378.
53. Houtekamer PL, Mitchell HL. Data assimilation using an ensemble Kalman filter technique. *Mon Weather Rev*. 1998;126(3):796-811.
54. Iungo GV, Santoni-Ortiz C, Abkar M, Porté-Agel F, Rotea MA, Leonardi S. Data-driven reduced order model for prediction of wind turbine wakes, *Journal of Physics: Conference Series*. IOP Publishing; 2015;625(1):012009.
55. Cortina G, Sharma V, Calaf M. Investigation of the incoming wind vector for improved wind turbine yaw-adjustment under different atmospheric and wind farm conditions. *Renewable Energy*. 2017;101:376-386.
56. Bozkurt TG, Giebel G, Poulsen NK, Mirzaei M. Wind speed estimation and parametrization of wake models for downregulated offshore wind farms within the scope of PossPOW project. *Journal of Physics: Conference Series*. IOP Publishing; 2014;524(1):012156.
57. Yang W, Court R, Jiang J. Wind turbine condition monitoring by the approach of SCADA data analysis. *Renewable Energy*. 2013;53:365-376.
58. Chowdhury S, Zhang J, Messac A, Castillo L. Unrestricted wind farm layout optimization (UWFLO): investigating key factors influencing the maximum power generation. *Renewable Energy*. 2012;38(1):16-30.
59. Chowdhury S, Zhang J, Messac A, Castilo L. Optimizing the arrangement and the selection of turbines for wind farms subject to varying wind conditions. *Renewable Energy*. 2013;52:273-282.
60. Gebraad PMO, Teeuwisse FW, Wingerden JW, et al. Wind plant power optimization through yaw control using a parametric model for wake effects—a CFD simulation study. *Wind Energy*. 2016;19(1):95-114.

**How to cite this article:** Hamilton N, Viggiano B, Calaf M, Tutkun M, Cal RB. A generalized framework for reduced-order modeling of a wind turbine wake. *Wind Energy*. 2018;1–18. <https://doi.org/10.1002/we.2167>